Journal of Materials Research and Technology 31 (2024) 3844–3859

Contents lists available at ScienceDirect

Journal of Materials Research and Technology

journal homepage: www.elsevier.com/locate/jmrt

Comparative analysis of crystal plasticity models in predicting deformation texture in IF-Steel

J. Ochoa-Avendaño [a,*], K. Sedighiani [b], J. Galan-Lopez [c], C. Bos [a,b], L.A.I. Kestens [a,c]

[a] Department of Materials Science and Engineering, Delft University of Technology, Mekelweg 2, Delft, 2628 CD, Zuid-Holland, Nederlands
[b] Tata Steel Research & Development, P.O. box 10000, IJmuiden, 1970 CA, Noord-Holland, Nederlands
[c] Metal Science and Technology, Department of Electromechanical, Systems and Metal Engineering, Ghent University, Technologiepark 46, IJmuiden, B-9052, Oost-Vlaanderen, Belgium

ARTICLE INFO

Keywords:
Texture
Crystal plasticity
IF-steel
Deformation texture
Rolling
Microstructure

ABSTRACT

In an industrial context, selecting an appropriate crystal plasticity (CP) model that balances efficiency and accuracy when modelling deformation texture (DT) is crucial. This study compared DTs in IF-steel after undergoing cold rolling reductions using different CP models for two input texture scenarios. Three mean-field (MFCP) models were utilised in their most basic configurations, without considering grain fragmentation or strain hardening, in addition to a dislocation-density-based full-field (FFCP) model. The study quantitatively compared the results from the MFCP models with those from the FFCP models. Furthermore, all CP model results were compared with experimental textures obtained from electron back-scatter diffraction (EBSD) experiments. The findings revealed that certain MFCP models could predict deformation textures as accurately as the FFCP models. Notably, one of the MFCP models exhibited a superior match with experimental textures for cold rolling reductions at 60%. Upon closer examination of specific crystallographic components, it was observed that MFCP models tended to predict a stronger {111}⟨211⟩ component, while the full-field model favours the {111}⟨011⟩ component. It is crucial to emphasise the importance of quantifying the texture within individual grains when assessing the macro-level deformation texture in rolling simulations.

1. Introduction

The crystallographic texture of cold-rolled and subsequently annealed steel sheets is a primary concern for steel manufacturing companies as a wide variety of mechanical and physical properties depends on it. In this regard, the quantitative prediction of deformation textures (DT) resulting from the cold-rolling process is crucial for optimising the steel sheet design and fabrication process since its characteristics are closely related to the final recrystallisation texture obtained during subsequent annealing [1]. For example, a specific crystal orientation might determine the recrystallisation texture if it has the required energy and mobility advantages with respect to neighbouring crystals in the deformed structure [2]. One approach to predict the DT is through Crystal Plasticity (CP) modelling [3]. In these models, rotation of individual crystals relies on their crystallographically resolved mechanical response when subjected to external loading so that the kinematics of the slip activity in every individual grain are quantified [4]. Several CP models have been developed, from the classic full-constraint Taylor (FCT) model [5,6], through the finite-elements-based models [7], to most recently the neural-network-based CP models [8].

These different CP models can be classified into mean-field (MFCP) and full-field (FFCP) models [9]. MFCP models assume that each grain in the material is subjected to homogenised boundary conditions and interacts with neighbouring crystals in a statistically averaged manner [10]. Thus, the DT is predicted by resolving the slip activities on individual crystal orientations under the applied (local or homogenised) conditions. Such a procedure allows to derive the crystal lattice spins for each strain increment and therefore to gauge the crystal lattice rotation with respect to an external reference frame [6]. On the other hand, in MFCP models, the topological description of the microstructure is not considered; instead, the input consists of a discrete set of orientations derived from the orientation distribution function (ODF) representing the material's initial texture [11]. This approach has several advantages in predicting DT in an industrial context. First, it is a computationally low-cost method that may provide sufficiently accurate results for specific applications. Second, the input is statistically representative of the actual initial texture prior to deformation [12]. Nevertheless, because topological parameters of the microstructure are not taken into account in considerate detail, some phenomena, such as grain

* Corresponding author.
E-mail address: j.f.ochoaavendano@tudelft.nl (J. Ochoa-Avendaño).

https://doi.org/10.1016/j.jmrt.2024.07.030
Received 29 March 2024; Accepted 7 July 2024
Available online 14 July 2024

interactions and deformation heterogeneity within grains, can only be considered by adding statistical topological information to the model that most often is not readily available, and therefore it is not trivial to implement in the MFCP framework. [13–15].

The FFCP models provide a detailed description of the material's mechanical behaviour by simulating deformation on the scale of individual grains. These simulations are conducted within a small homogenised portion of the material known as the representative volume element (RVE) [7]. The RVE is a virtual representation of the microstructure under consideration, and it is discretised in several number of elements at small-step spatial resolutions aiming to resolve the relevant microstructural features with sufficient accuracy [16]. Thus, the deformation process is simulated at every discrete element, reaching the full description of the strain and stress state for every element in the RVE [17]. In this way, complex phenomena, such as in-grain deformation heterogeneities and mechanical interactions between neighbouring grains, can be included in the simulation [18]. Therefore, the outcome of FFCP models is a complete description of the local stress and strain velocity fields, including the crystal rotation fields, capable of sufficient spatial resolution to allow for observation of intra-grain substructures [19]. However, FFCP models are difficult to apply in an industrial context due to their high computational cost [20]. Furthermore, although faster simulations can be performed by limiting the number of grains of the initial RVE, they might lead to an inaccurate statistical representation of the material's initial texture and microstructure [21].

Comparing the performance of MFCP and FFCP models to predict DTs has been addressed in previous works. For example, Hutchinson (1999) compared full-constraint and relaxed-constraint MFCP models to establish differences in the evolution of deformation texture and substructures. The results indicated that while relaxed-constraint models predict the existence of specific crystallographic components that full-constraint models do not capture, both types of models tend to predict textures with significantly higher intensities than those observed through experimental techniques. [22]. Bate and Quinta de Fonseca (2004) evaluated the prediction of DT in IF-steels by mean-field Taylor-type models against full-field Finite Element Method CP (FEMCP) models, providing a quantification of the differences for several strain levels. Their investigation led to the conclusion that, up to a strain of approximately 0.75, the FEMCP model provided better DT predictions than Taylor-type models. However, it is worth noting that FEMCP model fell short in capturing the increase in the spread of the $\alpha - fibre$ towards $\{001\}\langle 110\rangle$, which is a common observation at higher strains [23]. Liu et al. (2010) evaluated the prediction of DTs in FCC materials using different solvers in FFCP models, such as the fast Fourier transform-based and a finite element method-based model. Their study revealed that the fast Fourier approach successfully predicted the expected DT, when simulating with more than a thousand orientations and using a low-resolution RVE. In contrast, the performance of the FEMCP model appeared to be influenced by the input orientations used in the simulations, suggesting the necessity for a higher amount of orientations in the input of the RVEs in such cases [17].

Although prior studies have compared the overall deformation texture results produced by several CP models, uncertainties still need to be clarified regarding choosing a suitable model that balances efficiency and accuracy in an industrial application. Moreover, the impact of critical parameters on CP simulations, such as the level of grain interaction in MFCP, the sensitivity of MFCP to input texture, and the significance of in-grain texture in the ultimate macro texture outcome, continues to be an area requiring further investigation. Furthermore, it is essential to compare MFCP models with high-resolution FFCP models to evaluate the importance of capturing in-grain texture evolution versus having a precise statistical representation of the input texture on the final deformation texture result.

Table 1
Chemical composition of the IF-steel used in this study.

	C	Mn	Ti	N	Al
wt. [%]	0.002	0.13	0.065	0.004	0.05

This research analyses the disparities in DT predictions of an Interstitial-Free (IF) steel sheet cold rolled to different reductions from applying four CP models. The study employs a numerical quantification to gauge the degree of agreement between predicted DTs across various levels of deformation. It compares MFCP models to a FFCP model and evaluates all CP models by comparison with experimental results. The simulation scheme presented in this paper allows us to explore how the variations in the input texture affect the resulting DT within the MFCP models. Furthermore, insights into the evolution of specific ODF components in response to varying strain levels across all CP models are presented.

To gain a more detailed understanding of specific crystallographic components' evolution, we distinguish between the α and γ fibres. The four CP models studied include three MFCP models, i.e. the Full-Constraint Taylor (FCT) [24], the Advanced-LAMEL (ALAMEL) [25], and the Visco-plastic Self-Consistent (VPSC) [26] models in their more simplified setup, i.e. without grain fragmentation and strain hardening schemes. The fourth model, which corresponds to the FFCP model category, is a dislocation-density-based (DDB) model implemented in the Düsseldorf Advanced Material Simulation Kit (DAMASK) [27,28]. This model is used in a configuration that emphasises the role of in-grain texture evolution [19] on the macrotexture results, incorporating grain fragmentation. This present investigation unfolds through two distinct scenarios. First, in scenario-I, the performance of the three MFCP models is compared to that of the DDB model. In contrast, the second scenario, scenario-II, assesses the performance of all four models compared to experimentally obtained textures.

2. Experimental methods

2.1. Simulation scenarios description

The comparative study presented in this paper examines two distinct scenarios. In scenario-I, the goal is to compare the deformation texture predictions by the MFCP models with that of the DDB model. Scenario-II assesses the deformation texture predictions of all four models, MFCP and DDB, against experimentally obtained textures measured through EBSD experiments. The MFCP simulations in scenario-I and scenario-II differ in their input textures, while the DDB model simulations remain the same in both scenarios. Further details on the input textures are provided in Section 3.4.

2.2. EBSD experiments

The as-received materials are hot-rolled (HR) interstitial free (IF) steel plates ($thickness$ = 5 mm, $width$ = 60 mm) with the chemical composition provided in Table 1. Two plates were cold rolled on a laboratory rolling mill to achieve 60% and 77% thickness reductions. The crystallographic textures of the HR and cold-rolled (CR) sheets were measured using the electron back-scatter diffraction (EBSD) technique on samples extracted from the centre of the sheet. The surfaces aligned parallel to the plane formed by the sheet's regular and rolling directions (the ND-RD plane) were prepared for EBSD scans with OPS solution and electropolishing techniques. EBSD experiments were carried out on a FEI Quanta 450 scanning electron microscope. Data pattern collection was performed with OIM software Type EDAX-OIMvs. 8.6® at an acceleration voltage of 20 kV. The specimen tilt angle was 70°, and rectangular surfaces ($width$ = 200 μm, $length$ = 500 μm) were scanned with a step size of 0.7 μm on a hexagonal scan grid.

2.3. Macrotexture analysis

EBSD scanned data were used to calculate the Orientation Distribution Functions (ODFs) from individual orientations in Euler angles $g_i = \{\varphi_1, \Phi, \varphi_2\}$. ODFs were calculated using the generalised harmonic series expansion method proposed by Bunge [11], with $l_{max} = 22$. On each orientation pixel of the EBSD scan, a Gaussian ODF was centred with a spread of 10°, and all the Gaussian functions were superimposed to determine the overall ODF. The calculation of the ODFs was performed using MTEX software [29], without sample symmetry assumptions. The resulting ODFs are presented in the traditional $\phi_2 = 45°$ sections calculated in the triclinic domain, i.e. $0° < \varphi_1 < 360°$ and $0° < \Phi, \varphi_2 < 90°$. However, for the sake of clarity in visualisation, only the orthorhombic segments of these ODFs are presented. The ODFs were further analysed by considering the volume fractions of the $\alpha - fibre(\langle 110\rangle \parallel RD)$ and the $\gamma - fibre(\langle 111\rangle \parallel ND)$ with a tolerance of 10° with respect to the ideal skeleton lines. In the same way, partitions of specific crystallographic components were evaluated with 10° tolerance from the ideal orientations. Fig. 1 illustrates the positions of the crystallographic components and the fibres examined in this paper.

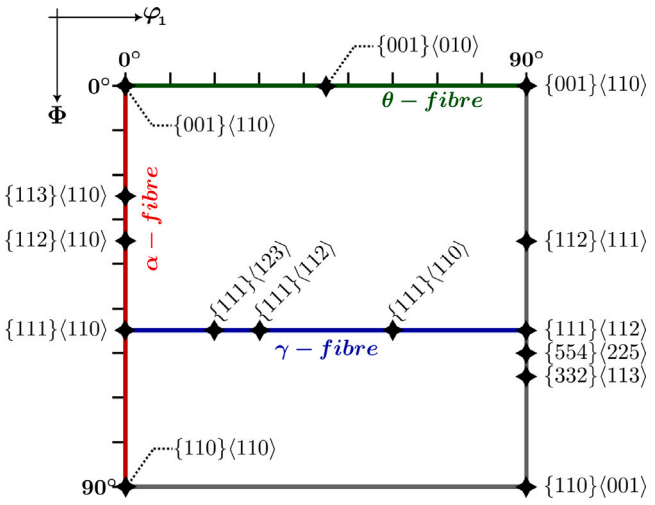

Fig. 1. Fibre textures and crystallographic components relevant for textures analysis in BCC alloys for rolling and annealing textures; $\varphi_2 = 45°$ section.

2.4. Texture comparison quantification

To quantify the difference between textures, the texture direct correlation, J_D, available in the ATEX software suite was used [30]. J_D ranges between 0 and 1. A value of 1 indicates a perfect match between the two ODFs being compared, while 0 indicates that there is no correlation. For two textures A and B, the ODFs are denominated by $f_A(g)$ and $f_B(g)$. Thus, the texture direct correlation J_D between $f_A(g)$ and $f_B(g)$ is defined as follows:

$$J_D = \frac{\int_g f_A(g) f_B(g) \mathrm{d}g^2}{\sqrt{\int_g f_A^2(g)\mathrm{d}g^2 \cdot \int_g f_B^2(g)\mathrm{d}g^2}} \tag{1}$$

In the present study, J_D values were calculated for simulation scenarios I and II and are presented in Sections 4.1 and 4.2.1, respectively. It is important to note that the J_D values cannot not be directly comparable between the two scenarios. This is because the J_D values in each scenario were calculated using different reference frameworks: MFCP results compared to DDB results in scenario-I, and all CP models compared to experimental results in scenario-II.

3. Crystal plasticity modelling

This section provides a brief overview of the fundamental principles of single crystal plasticity theory and outlines the key aspects of the four crystal plasticity models under consideration.

3.1. Single crystal plasticity theory

In CP theory it is assumed that plastic deformation mainly occurs by the activation of specific slip systems due to dislocation glide [7]. When the elastic strain component is neglected, the slip within a single crystal orientation g occurs on a slip system s in the direction $\overline{b^s}$ and on a slip plane with normal $\overline{n^s}$. Therefore, the rate of plastic deformation L_{ij}^g, on a slip system s, due to simple shear strain rate $\dot{\gamma}^s$ can be expressed as:

$$L_{ij}^g = b_i^s n_j^s \dot{\gamma}^s. \tag{2}$$

The kinematic equation that considers the activation of N slip systems on a single crystal for producing slip, is given by:

$$\dot{\varepsilon_{ij}} = \frac{1}{2}(L_{ij} + L_{ji}) = \sum_s^N \frac{1}{2}(m_{ij}^s + m_{ji}^s)\dot{\gamma}^s. \tag{3}$$

Where $\frac{1}{2}(L_{ij} + L_{ji})$ corresponds to the symmetric part of the velocity gradient L_{ij}, and $\frac{1}{2}(m_{ij}^s + m_{ji}^s)$ is the symmetric part of the Schmid tensor which indicates the slip direction and slip plane normal to each slip system s that might be activated to accommodate L_{ij}.

The lattice spin rate $\dot{\Omega}_{ij}$ is then defined as the difference between the macroscopically imposed velocity gradient L_{ij} and the velocity gradient that produces slip in the single crystal L_{ij}^g, such that $\dot{\Omega}_{ij} = L_{ij} - L_{ij}^g$. This difference is responsible for the orientation change of the single crystals, explained by the misalignment between the L_{ij} direction and the Schmid tensor in the single crystal m_{ij}^s. Therefore, the crystal rotation rate of a single crystal can be described by:

$$\dot{\Omega}_{ij} = L_{ij} - \sum_s^N m_{ij}^s \dot{\gamma}^s. \tag{4}$$

In Eq. (4), L_{ij} is imposed when the boundary conditions are given in terms of the velocity field, and it corresponds to the deformation modes applied to the material, this is known as the first Taylor hypothesis. The term m_{ij}^s is known, and depends on the crystal structure. In BCC materials m_{ij}^s is defined by the 48 different potential slip systems corresponding to the pencil-glide slip. In the present work, however, only the slip systems {110}⟨111⟩ and {112}⟨111⟩ were considered, yielding 24 slip systems in total. This selection was made based on previous observations indicating that slip predominantly takes place in 110 planes during room temperature deformations [31].

From a continuum mechanics perspective, a rolling operation can be approximated by a plane strain compression velocity field of which the velocity gradient tensor is given by:

$$\left[L_{ij}\right] = \begin{bmatrix} 1 & 0 & 0 \\ 0 & 0 & 0 \\ 0 & 0 & -1 \end{bmatrix} \dot{D}_0. \tag{5}$$

In this case L_{ij} is expressed as the tensor that characterises the prescribed strain mode, multiplied by the macroscopic scalar measure of the strain rate $\dot{D}_0$. In this paper the boundary conditions imposed during rolling simulation will be characterised by the velocity gradient tensor of Eq. (5).

3.2. Mean-field crystal plasticity modelling

3.2.1. FCT model description

The first Taylor hypothesis holds that all discrete orientations of a polycrystalline aggregate are locally subjected to the same velocity gradient as the macroscopic workpiece [4]. Thus, the FCT model respects perfect strain compatibility at grain boundaries but violates stress equilibrium [25]. The second Taylor hypothesis assumes that a

set of crystallographic slip systems is activated if it geometrically complies with the boundary conditions but also minimises the plastically dissipated power.

In the present application, it was assumed that the critical resolved shear stresses (CRSS) on all slip systems are identical as commonly assumed for BCC materials [32], and no strain hardening was considered. Despite these simplifying assumptions, there are numerous cases where the DT predicted with the FCT model agrees with experimental results [6] in an acceptable manner. The FCT rolling simulations were applied by considering the ($\{110\}\langle 111\rangle$ and $\{211\}\langle 111\rangle$) slip systems. It is considered that the strain rate $\dot{D}_0$ takes a value of $0.01\,s^{-1}$, whereby macroscopic strains are modelled by recurrent accumulation of small strain increments. In the present study, the FCT model as implemented by Van Houtte [24] was applied. In the Van Houtte approach, the Taylor optimisation problem for determining the active slip systems is solved by a linear programming method [6].

3.2.2. ALAMEL model description

Prior investigations on improving the prediction of DT during rolling processes revealed that incorporating grain interactions and relaxing the geometric constraints imposed by the FCT model could lead to more accurate results [33,34]. In the ALAMEL model by Van Houtte et al. [25], it is considered that the polycrystalline aggregate consists of a set of clusters formed by pairs of two crystal orientations and a vector $\vec{\boldsymbol{V}}_{\boldsymbol{GB}}$ representing the normal to a virtual grain boundary plane separating the two orientations. The macroscopic velocity gradient L_{ij} is imposed for each cluster, and additional shear strains along the common grain boundary are introduced with equal magnitudes but opposite in signs (cf. Fig. 2(*a*)). Consequently, the sum of the additional shear relaxations is zero, and the shear stress equilibrium at the grain boundary is satisfied. This means that the resolved shear stresses at the common grain boundary from the two neighbouring grains are equal. Additionally, the induced velocity field near the boundary interface partially solves the lack of local interaction of the FCT model [35], see Fig. 2(*b*).

Correspondingly, the configuration of the clusters formed in the ALAMEL model, i.e. misorientation between the pair of orientations and the assignation of the $\vec{\boldsymbol{V}}_{\boldsymbol{GB}}$ vector, implicitly introduces a topological aspect in the simulations. This characteristic makes ALAMEL a nondeterministic model, resulting in an outcome variability that can be attributed to two primary factors. Firstly, in the ALAMEL algorithm, grain pairing is determined based on the ordered list of input orientations, and second, the vector $\vec{\boldsymbol{V}}_{bold\,symbol GB}$ is randomly assigned to each grain pair. As a result, alterations in the sequence of input orientations and the randomness $\vec{\boldsymbol{V}}_{\boldsymbol{GB}}$ vectors may influence the final texture predicted by the ALAMEL model. Consequently, this study conducted five ALAMEL simulations for each strain level, varying the order of input orientations and grain boundary vectors. Therefore, results related to the ALAMEL model are presented with confidence intervals.

The ALAMEL rolling simulations were performed by considering $\{110\}\langle 111\rangle$ and $\{112\}\langle 111\rangle$ slip systems. All CRSS values are equal for all slip systems, no strain hardening is assumed and $\dot{D}_0 = 0.01\,s^{-1}$. The precise details of the model algorithm can be found in Ref. [25].

3.2.3. VPSC model description

In the VPSC model developed by Lebensohn and Tomé [26], every single orientation is treated as an inclusion embedded in a homogeneous effective medium; an approach inspired by the Eshelby methodology for ellipsoidal inclusions [36]. In this way, the VPSC model assumes that the polycrystalline overall stress and strain rate influence the grain deformation, effectively considering a long-range interaction between each specific grain and the homogenised surrounding matrix [37]. The properties of the surrounding matrix are updated for each deformation step, and iterative convergence algorithms are necessary to achieve the Self-Consistent formalism in the slip activity calculations [38,39].

Similar to other MFCP models, VPSC predicts textures with higher intensities than expected since no local interactions are considered. In real materials, grains with similar orientations may deform differently in response to their local behaviour. However, in the VPSC model, these grains will follow the same interaction law and thus rotate to exactly the same final orientation [20]. Various authors have developed enhanced VPSC-based models that integrate local grain interaction in response to this limitation. Notable developments include the cluster-type VPSC approach by Van Houte et al. [40], and a VPSC version incorporating local interaction developed by Lebensohn et al. [41]. At the same time, grain fragmentation was addressed by Zecevic et al. [42]. Furthermore, strain hardening can be incorporated in the VPSC model, whereby different hardening models can be implemented [43–45].

In this study, the grain fragmentation was not considered, whereas a simple Voce hardening law was implemented, with the parameters $\tau_0 = 2.0$, $\tau_1 = 0.0$, $\theta_0 = 0.0$, $\theta_1 = 0.0$. These parameters imply that the critical resolved shear stresses (CRSSs) remain constant for all slip systems. The simulations used the same slip systems as those used in the FCT and ALAMEL models, with a strain rate of $\dot{D} = 0.01\,s^{-1}$.

The grain co-rotation scheme from the VPSC model to handle grain reorientation resulting from interactions with adjacent grains was included in the simulations as outlined by Tome et al. (2023) [46]. This scheme was applied based on the approach presented by Takajo et al. (2018), where the effective number of neighbouring grains, denoted as N_{neigh}, changes with the final rolling reduction percentage R following the formula: $N_{neigh} = \mathrm{int}(3.5 + 1.5\tanh(5\ln(1-R) + 3.6))$ [32]. Additionally, the rate sensitivity, as defined in [47], was set at $n = 20$, following the approach used in previous studies [32]. The simulations were performed using an elasto-visco-plastic version of the original VPSC model [26], specifically, the VPSC90 model developed by Galan et al. [38].

3.3. High-resolution full-field crystal plasticity modelling

This paper employed a dislocation-density-based (DDB) model [18,27] to carry out the FFCP simulations. The simulation involved a high-resolution RVE comprising 36 grains to investigate the evolving deformation heterogeneity and misorientation features during large strain deformation, as depicted in Fig. 3. The crystallographic orientations of the grains are sampled from the EBSD map of the as-received material. It is worth noting that 36 grains may not fully represent the initial texture statistically. Consequently, the evolving texture is anticipated to diverge from the experimental DT, especially at small strains.

The model was implemented in the open-source software DAMASK (Düsseldorf Advanced Material Simulation Kit). DAMASK is a multi-physics simulation toolkit with several crystal plasticity models that use different solvers to address mechanical boundary value problems. Further details can be found in [27,48]. The Fast Fourier Transform based on the spectral method [49,50] of DAMASK was used to conduct the CP simulations using a DDB constitutive law.

The high-resolution RVE was subjected to plane-strain compression at a strain rate of $100\,s - 1$ up to a total thickness reduction of 77% ($\varepsilon = 1.47$). Initially, there were approximately 34 000 elements per grain, gradually increasing to 550 000 per grain during deformation through a multistep mesh refinement method outlined in [19]. Therefore, at the final stages of the deformation, each grain is discretised using around 550,000 elements. This substantial number of elements per grain facilitates the prediction of strain gradients and deformation heterogeneities within each grain.

Conducting simulations of large deformations within the FFCP framework can result in problems related to mesh distortion. To avoid these issues, the re-meshing technique proposed by Sedighiani et al. [51]

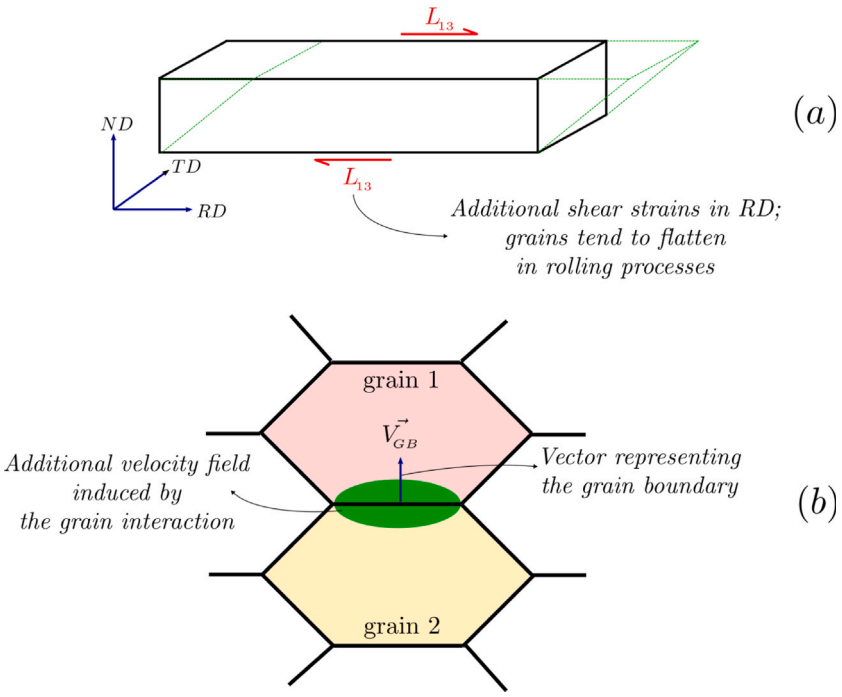

Fig. 2. ALAMEL model representation, (a) additional shear strains in RD to emulate flattening of grains during rolling process, (a) cluster assembly for texture evolution calculation, the induced velocity field near the boundary interface creates a virtual grain interaction.

is employed. This methodology uses a nearest-neighbour mapping algorithm to replace distorted meshes with new undistorted ones. The state variables are mapped from the deformed stage onto the new mesh. Subsequently, the simulation is restarted as a new simulation, with the initial state set based on the last deformation state reached.

During large deformation, elements' aspect ratio (the ratio of the element size in the stretching direction to that in the compression direction) can become notably large. Extensively elongated elements not only introduce errors in the simulation but can also impede strain localisation. These errors are mitigated using a multi-step mesh refinement approach to update mesh density during deformation at each re-meshing step [19]. This strategy aims to maintain a constant number of elements in the compression direction while adjusting the number in the stretching direction to preserve cubic-shaped elements. The gradual increase in elements and mesh resolution during deformation ensures minimal information loss during mapping, with a minimal increase in the number of simulation points [19].

Fig. 3(*a*) presents IPF maps parallel to the loading (vertical) direction in the mid-surface of the DDB simulation for various thickness reductions. Fig. 3(*b*) shows the $3D$ IPF map for the same RVE after a 77% ($\varepsilon = 1.41$).

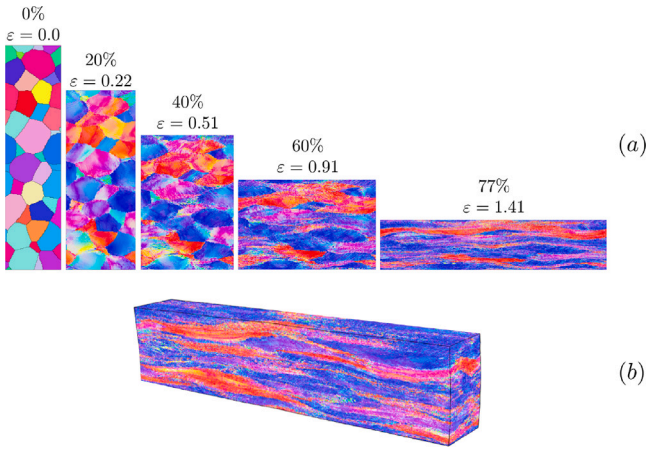

Fig. 3. IPF maps for the DDB model simulations. (a) maps parallel to the loading (vertical) direction in the mid-surface at different thickness reductions. (b) the 3D IPF maps after 77% thickness reduction.

3.4. Input textures description

In this work, the RVE for the DDB simulations consists of 36 grains sampled from the hot rolled microstructure (see Fig. 4). The crystallographic orientation for every sampled grain is assigned based on the methodology proposed by [52], resulting in the ODF presented in Fig. 4 - texture (*a*). The DDB simulations, as described in [28], aimed to provide a detailed model of localised deformation within grains. A very high-resolution RVE was necessary to achieve this, as suggested by previous studies [51,53]. Additionally, conducting FFCP simulations at significant strain levels often leads to distortion in the RVE's mesh, a problem addressed through re-meshing techniques [51, 54]. Consequently, for the DDB simulations presented in this work, high-resolution RVE and re-meshing techniques were required. These constraints led to the use of an input texture derived from only 36 grains.

The MFCP simulations were performed over discrete sets of orientations [55]. The ODFs representing the material before the deformation process were discretised according to the cumulative ODF statistical technique (STAT), proposed by Toth and Van Houte [56] (see textures (*b*) and (*d*) in Fig. 2). The STAT technique is based on calculating the cumulative ODF (F(G)), which is defined as the integral of the ODF along any integration path across the entire orientation space:

$$F(G) = \int_{G_0}^{G} f(g)dg. \tag{6}$$

In this context, G represents a crystallographic orientation that serves as the centre point for discretising Euler space into a regular grid, often with a resolution of 5°. This central point is associated with an individual orientation $g_i = \{\varphi_1, \Phi, \varphi_2\}$, and it also includes the integral of the ODF within the corresponding grid box, denoted as $f_i = \int_{box_i} f(g)dg$.

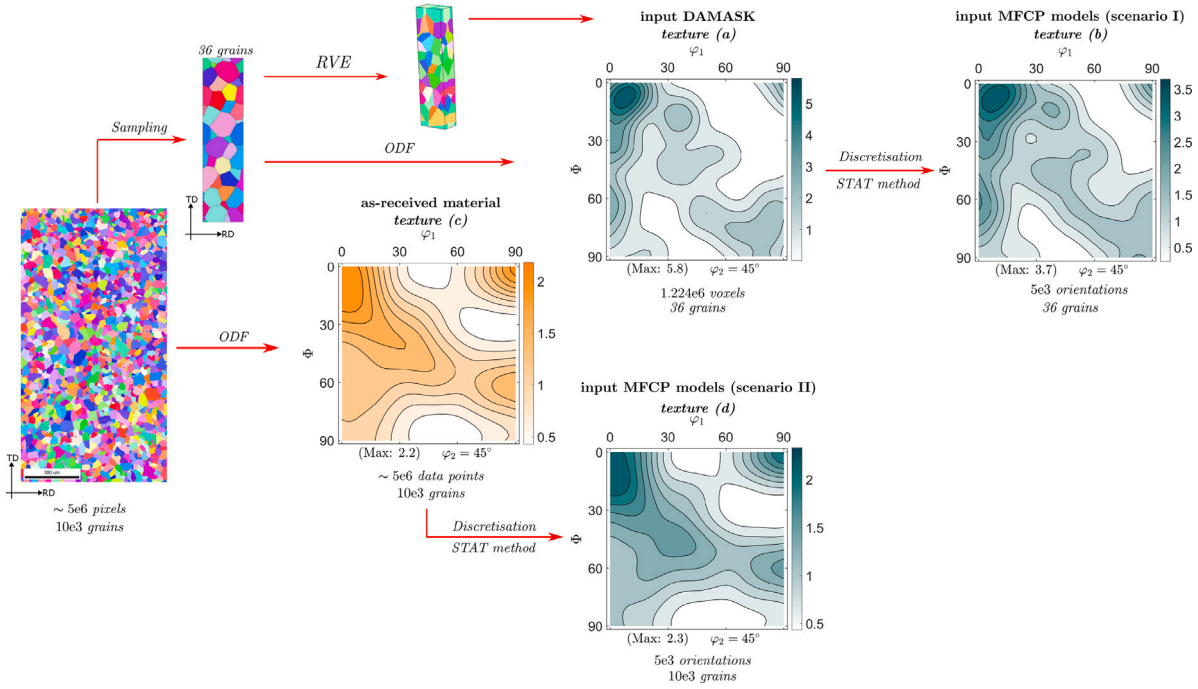

Fig. 4. Texture (*c*): experimentally measured ODF of the as-received material. Texture (*a*): input texture for DDB simulations. Texture (*b*): ODF discretised from texture (*a*) with STAT method, the input for FFCP simulations in scenario-I. Texture (*d*): ODF discretised from texture (*c*), the input for FFCP simulations in scenario-II.

A cumulative distribution function denoted as $F(j)$ is constructed for integer values of j. This function is defined as $F(j) = \sum_{i=1}^{j} f_i$. Graphically, it takes the form of a stepwise function, which can be further discretised using a set of n selectors denoted as s_k ($n = 5000$ in this work). A discrete orientation i, which is computed using the STAT method as described in the work by Toth (1992) [56], corresponds to each selector.

The input texture for the MFCP scenario-I (see Fig. 4 texture (*b*)) is a set of 5000 orientations obtained by discretising the DDB input texture (i.e. Fig. 4 texture (*a*)). Scenario-I aims to compare the performance of the MFCP models with the DDB model. Thus, a texture with a typical number of orientations representing the 36 grains of the RVE in DDB was needed to carry out the MFCP simulations with the same starting conditions as the DDB model. In scenario-II the objective is to compare the performance of each CP model with the experimental EBSD results. Therefore, an input texture representing the initial condition of the as-received material (Fig. 4 texture(*c*)) is required. The input texture for MFCP scenario-II (i.e. Fig. 4 texture (*d*)) corresponds to a set of 5000 orientations obtained by the discretisation of the ODF calculated from the EBSD measured on the IF-steel in as-received condition (Fig. 4 texture (*c*)).

By comparing textures (*a*) and (*d*) with texture (*c*) in Fig. 4, it can be observed how different the discrete input textures are compared to the experimentally measured input texture (see Fig. 10 for $\varepsilon = 0.0$). Self-evidently the representation employing 5000 orientations discretised from the EBSD measured ODF better resembles the experimental data, in contrast to the sample comprising 36 grains used in the DDB simulations, see Section 3.4. By comparing the deformation texture (DT) results from scenarios I and II, the proposed modelling procedure also allows for evaluating the sensitivity of models to the input texture. However, this comparison only applies to MFCP models since DDB simulations remain the same in scenarios I and II.

4. Results

Rolling reduction simulations of 20%, 40%, 60% and 77%, corresponding to plane strain CP simulations at $\varepsilon = 0.22$, $\varepsilon = 0.51$, $\varepsilon = 0.91$ and $\varepsilon = 1.46$ (true logarithmic strain), respectively, were performed with three different MFCP models: FCT, ALAMEL and VPSC. Two distinct inputs were employed, as explained in Section 3.4. Detailed description and parameters of the MFCP simulations for each model are provided in Section 3.2. The results from the DDB in scenario-I and scenario-II are the same, since they used the same input texture. To compare the DT predictions derived from all CP models with respect to EBSD results, only the strains $\varepsilon = 0.0$, $\varepsilon = 0.91$ and $\varepsilon = 1.46$ were considered. These results were compared with the EBSD measured textures corresponding to as-received condition 0%, 60% and 77% cold rolled reductions, respectively.

4.1. Scenario-I

4.1.1. Texture direct correlation

Fig. 5 displays the comparative performance of the VPSC, ALAMEL, and FCT models with respect to the DDB model; the ODFs resulting from scenario-I for the different strain levels are presented in Appendix A. The FCT and VPSC models show a decreasing resemblance to the DDB result with increasing rolling strains, whereas the ALAMEL model initially shows a relatively low J_D at $\varepsilon = 0.22$ simulation and then increases its J_D values at higher strain levels. Notably, at a strain value of $\varepsilon = 1.46$, the ALAMEL and VPSC models produce virtually identical direct correlation with respect to the DDB result, $J_D = 0.936$ and $J_D = 0.934$, respectively. However, this does not imply that for $\varepsilon = 1.46$ ALAMEL and VPSC predict identical textures. As displayed in Fig. 6, the ALAMEL result differs from VPSC result mainly in the prediction of the $\alpha - fibre$. The ALAMEL model predicts the highest intensity on the $\{113\}\langle 110\rangle$ component, while for the VPSC simulations the $\{111\}\langle 110\rangle$ and the $\{001\}\langle 110\rangle$ components are the most intense on the $\alpha - fibre$. Regarding the $\gamma - fibre$, the MFCP models display the highest intensity on $\{111\}\langle 112\rangle$ while the DDB model predicts the maximum intensity on the $\{111\}\langle 110\rangle$ component. More details on these characteristics can be found in Appendix C.

4.1.2. ODF maximum intensities

Fig. 7 illustrates the variation in ODFs maximum intensities for the different simulated strain levels. All three MFCP models generally

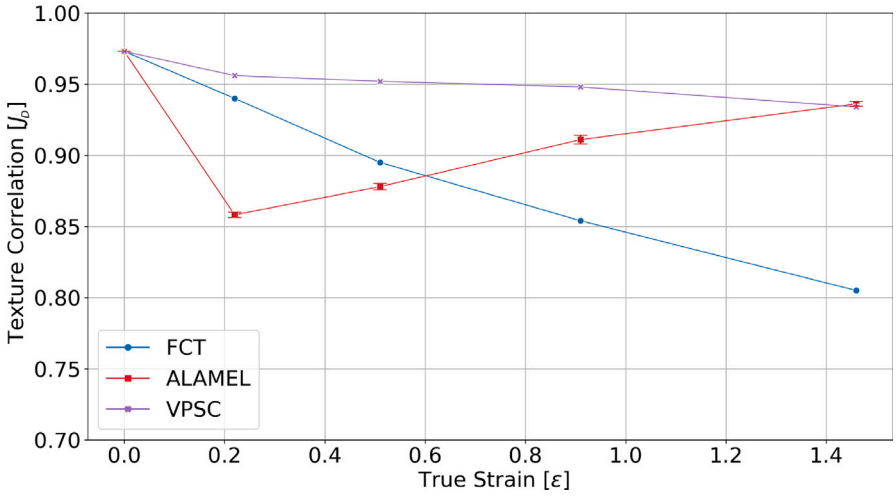

Fig. 5. Texture direct correlation [J_D] for scenario-I. Texture correlation quantification between deformation textures obtained with the MFCP models with respect to DDB model results. [J_D] as a function of the equivalent strain.

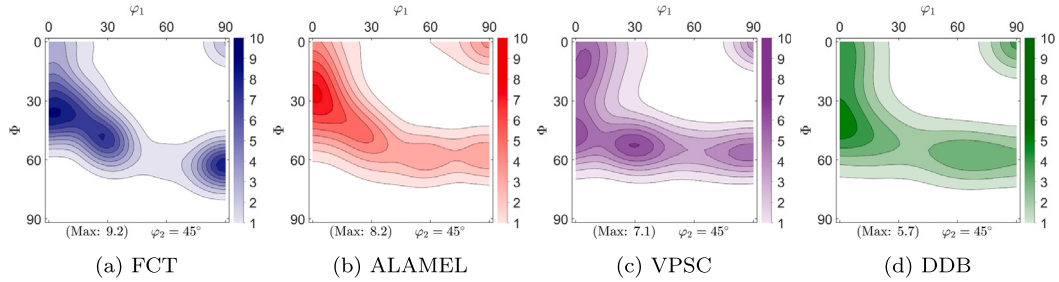

Fig. 6. ODFs sections at $\phi_2 = 45°$ resulting from scenario-I, plane strain compression $\varepsilon = 1.46$.

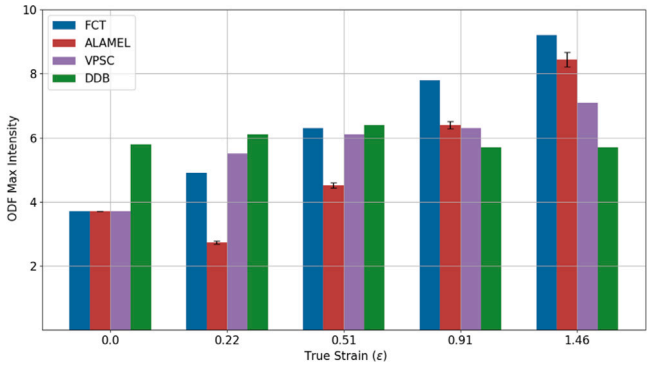

Fig. 7. ODF maximum intensities resulting from scenario-I.

exhibit an increment in ODFs intensities with increasing deformation, except for the ALAMEL model where it decreases when ε increases from 0.0 to 0.22. Comparing the MFCP models, VPSC displays the closest resemblance to the DDB predictions. Moreover, the graph indicates a trend whereby higher levels of grain interaction in the CP models correspond to lower values of the ODF maximum intensity, ranging from no grain interaction for the FCT model to full interaction in the DDB model. Notably, unlike the MFCP models, the maximum intensity of the DDB predictions increases for deformations ranging from $\varepsilon = 0.0$ to $\varepsilon = 0.51$ and then drops for $\varepsilon = 0.91$ and remains constant for further deformation up to $\varepsilon = 1.46$.

4.2. Scenario-II

4.2.1. Texture direct correlation

Fig. 8 displays the performance of the four CP models in predicting the DT texture compared with experimentally measured textures; all the ODFs compared are presented in Appendix B. First, it can be observed that prior to deformation ($\varepsilon = 0.0$), the procedure to represent the input texture (i.e. a discretised set of 5000 individual orientations obtained by discretising the ODF derived from the EBSD measurement) did not produce any noticeable deviation as the sampled and the measured texture are perfectly correlated with $J_D \approx 1.0$. In contrast, the DDB input texture, as it was restricted to a sample of only 36 orientations, see Section 3.4, shows a lower correlation of $J_D = 0.74$. As expected, α and γ fibres are present in all the simulations and, overall, all CP models predict a DT in reasonable agreement with the experimental results. For deformation up to $\varepsilon = 0.51$, all DTs resemble their respective initial textures, although for MFCP models it can be seen that the $\{001\}\langle 110\rangle$ component becomes weaker whereas this component increasingly intensifies in the experimental data. The DDB model improves its correlation with respect to the experimentally measured EBSD texture for high deformation levels, while the FCT model increasingly deviates from EBSD results for higher deformations.

At $\varepsilon = 0.91$, the VPSC model exhibits the closest correlation with the EBSD measured texture, while ALAMEL and DDB exhibit similar correlation values of $J_D = 0.853$ and $J_D = 0.866$, respectively. However, these ODFs have clear differences (see Appendix B). For example, the MFCP models better predict the $\gamma - fibre$ since it shows maximum intensities on $\{111\}\langle 112\rangle$ component, similarly to the EBSD results. In contrast, the DDB model shows the maximum component of the $\gamma - fibre$ on the $\{111\}\langle 110\rangle$ component. In the case of the $\alpha - fibre$, EBSD

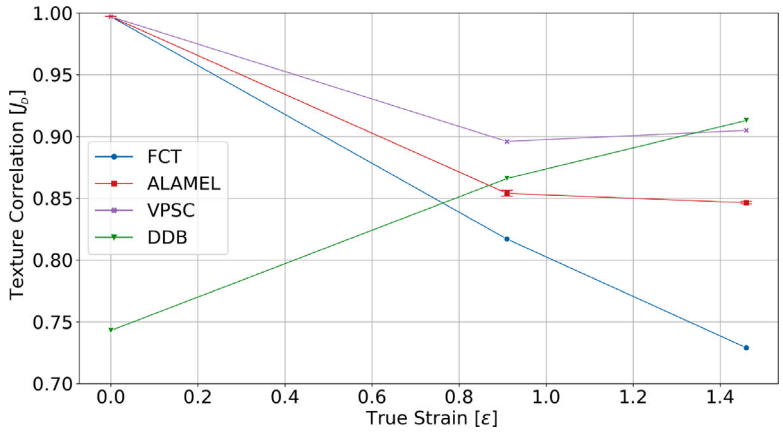

Fig. 8. Texture direct correlation [J_D] for scenario-II. Texture correlation quantification between deformation textures obtained with every CP models with respect to experimentally measured deformation textures. [J_D] as a function of the equivalent strain.

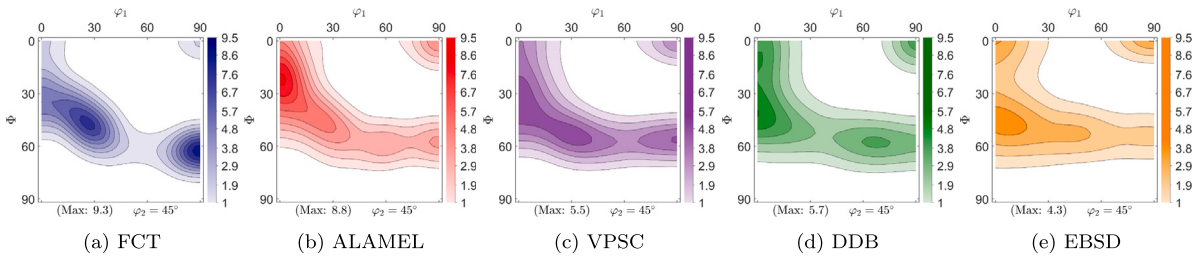

Fig. 9. ODFs sections at $\phi_2 = 45°$ resulting from scenario-II, plane strain compression $\varepsilon = 1.46$.

results show a clear intensification of the $\{001\}\langle 110\rangle$, component, which is only predicted by the DDB model, albeit with a minor deviation (see Appendix B).

For the strain of $\varepsilon = 1.46$ (see Fig. 9), the DDB model displayed the best correlation with EBSD results with $J_D = 0.913$, closely followed by the VPSC model with $J_D = 0.905$. However, these two models show noticeable qualitative differences in the predicted ODFs, as can be seen in Figs. 9(c) and 9(d) respectively. The ALAMEL result showed a correlation of $J_D = 0.847$, which still indicates a reasonable correspondence. As expected, the FCT model presented the lowest correlation with $J_D = 0.729$. When singling out the $\alpha - fibre$, it is observed that none of the models showed maximum intensities on the $\{001\}\langle 110\rangle$ component as in the EBSD result (see Appendix D). Another important distinction between the EBSD result and the four CP model results is that the $\alpha - fibre$ exhibits non-zero values up to $\Phi = 83°$ in the EBSD result, while in the CP models the maximum Φ value with non-zero intensity is 70°. In the case of the $\gamma - fibre$, it can be seen that the MFCP models and EBSD results present a stronger $\{111\}\langle 112\rangle$ than $\{111\}\langle 110\rangle$ component, while the DDB results exhibits a stronger $\{111\}\langle 110\rangle$ component as compared to $\{111\}\langle 112\rangle$, (see Appendix D).

4.2.2. ODF maximum intensities

Fig. 10 illustrates the variation in the ODF maximum intensities for the different simulated strain levels in scenario-II. Overall, for the three MFCP models, the maximum intensity increases with increasing deformation. The FCT and ALAMEL models displayed too high intensity maxima compared with EBSD results. Particularly for a deformation of $\varepsilon = 1.46$, the predicted value exceeds twice the experimentally observed

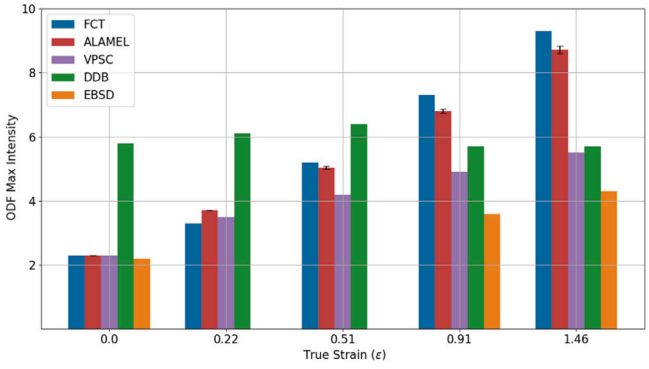

Fig. 10. ODF maximum intensities resulting from scenario-II.

maximum intensity. Interestingly, the VPSC model showed the closest values to the EBSD result for the strains of $\varepsilon = 0.91$ and $\varepsilon = 1.46$. Similarly to the observation of scenario-I, the higher the level of grain interaction in the MFCP models the lower the maximum intensities of the resulting ODFs.

4.3. Sensitivity of the input texture

The two simulation scenarios provide results that allow for evaluating the impact of the input texture on the results of the DT predicted by MFCP models for different strain levels. Fig. 11 shows the texture direct

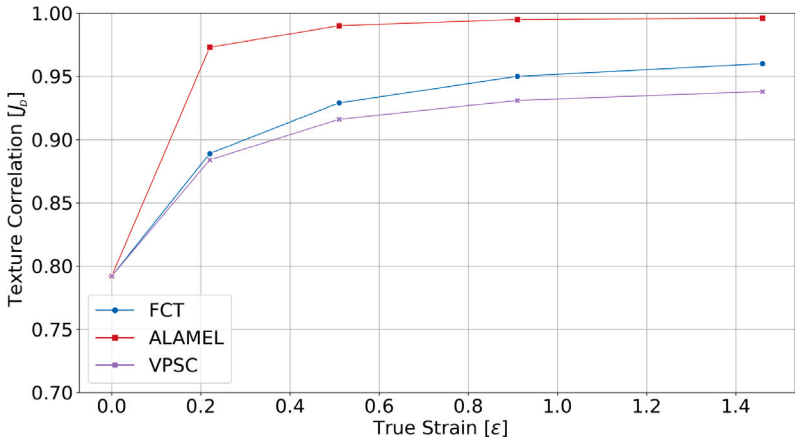

Fig. 11. Texture direct correlation [J_D] for deformation textures for the MFCP models. Comparison between deformation results obtained in scenario-I and scenario-II. [J_D] as a function of the equivalent strain.

correlation J_D between the results obtained in scenario-I and those obtained from scenario-II as a function of the strain level, whereby the only difference between the two scenarios is the difference in the initial texture. In the initial condition ($\varepsilon = 0.0$) the correlation is relatively low, $J_D = 0.792$, indicating the disparity of the input ODFs, cf. Section 3.4. As the strain levels increase ($\varepsilon > 0.0$), the correlation indices also rise, implying that the MFCP models tend to yield similar output ODFs for the different input textures examined here. The direct correlation values for the ALAMEL model indicate that this model is less sensitive to the input ODF. This observation is evident from Fig. 11, where the J_D values for ALAMEL are close to 1.0 from the strain $\varepsilon = 0.22$ onwards.

Although the ALAMEL model presented the least sensitivity to the input texture out of the other MFCP models evaluated in this paper, there is evidence suggesting that the arrangement of orientation pairs in ALAMEL, based on the actual topological characteristics of the microstructure (partially revealed, for instance, through EBSD data), can influence the resulting texture in rolling simulations [12,57]. Notably, result variability can be reduced when the input is not highly structured, the input orientations are randomly ordered, and the initial grain shape morphology is nearly equiaxed. This implies that the vectors $\vec{V}_{GB}$ are randomly distributed in space.

The input texture of the MFCP in scenario-I exhibits two distinct components (see Fig. 12). These components are approximately located at the Euler angles $[\phi_1 = 9.0°, \Phi = 7.0°, \phi_2 = 45.0°]$ and $[\phi_1 = 0.0°, \Phi = 65.0°, \phi_2 = 45.0°]$ and will be referred to as components x and y, respectively. The x component showing the maximum intensity in the input texture appears to rotate towards the $\alpha - fibre$ component $\{112\}\langle 110\rangle$ in FCT and $\{113\}\langle 110\rangle$ in ALAMEL. Also, the y component rotates to $\{112\}\langle 110\rangle$ and $\{113\}\langle 110\rangle$ in the FCT and ALAMEL models, respectively. On the other hand, both components x and y remain present in the VPSC result at all strain levels, with the y component appearing to rotate towards $\{111\}\langle 110\rangle$ component.

In the case of scenario-II, the input texture for the MFCP models exhibits a rotated cube component, $\{001\}\langle 110\rangle$, which gradually weakens with increasing strain levels in the MFCP simulations (see Appendix D). This weakening effect is particularly notable in the case of FCT. In both VPSC and FCT models, the rotated cube component appears to rotate towards the $\alpha - fibre$ component $\{112\}\langle 110\rangle$, while in ALAMEL, the rotation occurs towards $\{113\}\langle 110\rangle$. Furthermore, it is evident that the $\{111\}\langle 112\rangle$ component present in the input texture is relatively stable at all strain levels for all MFCP models, matching observations

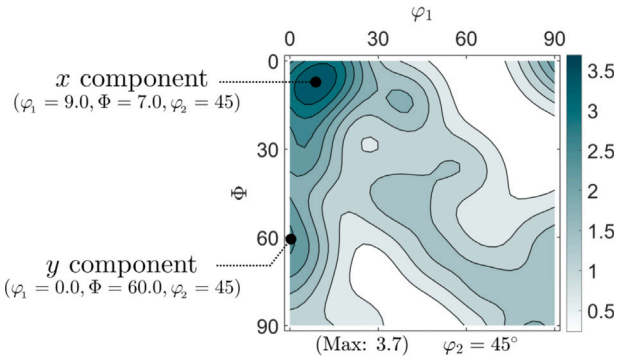

Fig. 12. Input texture scenario-I MFCP models.

in the EBSD results. For the DDB simulations, the aforementioned x component appears to rotate towards the $\alpha - fibre$ up to $\varepsilon = 0.91$ and disappears for $\varepsilon = 1.41$. The y component seems to rotate towards lower values of Φ, reaching $\Phi \approx 50°$ for $\varepsilon = 1.41$.

In the MFCP models (scenario-II), the maximum intensities of the deformation textures surpass those of the input texture at all strain levels, consistent with the observations in experimentally measured ODFs. However, DDB result deviates from this pattern, as the maximum intensity value of the input texture remains relatively unchanged even at high strain levels. Furthermore, for the DT results at $\varepsilon = 1.41$, the DDB model exhibits a slightly lower maximum intensity than that of the input texture, contrary to the behaviour observed in the MFCP models and EBSD results.

5. Discussion

Compared to the DDB model, the MFCP models can reasonably deal with a statistically relevant discrete sample of the input texture. The distinction becomes evident when examining the input textures in Fig. 13. Namely, the maximum intensity of the ODF in the input textures on which the DDB model is applied is much higher than the one of the experimentally observed input texture. This discrepancy can be attributed to the limited number of grains ($n = 36$) selected for the RVE in the DDB model input to represent the as-received material. The main reason for choosing an RVE with a limited number

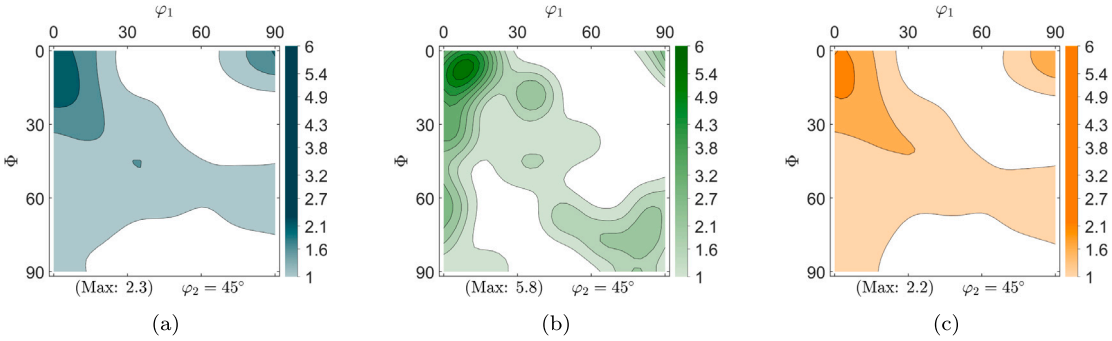

Fig. 13. Input textures for the CP simulations. (*a*) input ODF for MFCP scenario-II. (*b*) input ODF for DDB simulation scenario-I and II. (*c*) Experimentally measured ODF of the as-received material.

of grains was the need to discretise the RVE at high resolution. Since the primary objective of the DDB model was to investigate the in-grain microstructural evolution [28], a detailed discretisation of each grain was required as input for the simulation. This, however, implies a high computational cost, which is a limitation when performing high-resolution DDB simulations on large-size RVEs.

To put it in perspective, a DDB model simulation, such as the one considered in this work, demands approximately one week of computation on a workstation with 16 CPUs [28]. However, although the input texture for the DDB simulations did not closely resemble the experimentally measured one, given the small number of initial crystal orientations, the DT results obtained with the DDB model exhibited strong alignment with the experimentally observed DTs, particularly at medium to large strains. This observation highlights the significance of quantifying the texture within individual grains when determining the deformation texture at the macro level.

Conversely, the DDB simulations can be conducted within RVEs that incorporate a larger number of grains while employing a lower resolution in the spatial discretisation (DDB low-resolution). This choice aims to mitigate computational costs while still achieving DTs that closely align with experimental observations. However, this approach may overlook the detailed characterisation of orientation gradients within the grains. An illustrative example of such a simulation can be found in the work by Sedighiani [58]. In contrast, MFCP simulations do not face these computational challenges and can efficiently predict DTs involving thousands of orientations within minutes on a standard state-of-the-art laptop. Nevertheless, it is important to note that while MFCP models excel at predicting the DT, they do not describe the microstructural evolution.

As mentioned in Section 4.1, the maximum intensity predicted by the DDB model shows a slight increment from undeformed condition $\epsilon = 0.0$, until $\epsilon = 0.51$ after which it decreases for further strain levels, unlike the MFCP models and the EBSD textures displayed, cf. Fig. 10. Prior research has shown that MFCP models often predict higher intensity DTs compared to both FFCP predictions and experimentally observed textures [23,59]. This discrepancy arises because MFCP models typically represent each grain's crystallographic orientation with a single crystal orientation, while FFCP models, which incorporate grain fragmentation, introduce intragranular misorientation gradients. These gradients mitigate the occurrence of high peak intensities in the ODF [42,60]. This fundamental difference in the modelling approach explains the difference in texture intensity between the MFCP models and the full-field DDB model. However, the subsequent decrease in the maximum intensity within DDB for higher equivalent strain levels (after $\epsilon = 0.51$) may suggest an overestimation of grain fragmentation in the DDB model. Furthermore, the maximum intensity values of ODFs resulting from DDB simulations at various strain levels exhibit minimal fluctuations relative to their input texture. This observation might suggest a strong dependency of the maximum intensity predicted by the DDB model and the maximum intensity of its initial texture.

When evaluating the performance of all CP models, it was observed that the DDB model produced the closest texture prediction to the experimentally measured one for a strain of $\epsilon = 1.41$. This result is surprising, considering that the DDB model started the simulation from an initial texture that did not even closely resemble the experimentally measured input texture (see Fig. 13). Nevertheless, for a strain of $\epsilon = 0.91$, the VPSC model exhibited a better correlation between the predicted DT and the experimentally measured one. Furthermore, despite accounting neither for grain fragmentation effects nor strain hardening effects, the VPSC model's prediction for $\epsilon = 1.41$ was almost as precise as the DDB model. Similarly, the ALAMEL model's result for $\epsilon = 0.91$ was nearly as precise as the DDB's. This indicates the potential for further enhancement in the predicted DT results by incorporating additional phenomena, such as local topology of grain interaction, grain fragmentation, and strain hardening in a statistical manner in these two models.

As mentioned in Section 4.2.1, the texture direct correlation (J_D) of VPSC and DDB with respect to the EBSD result, for scenario-II at $\epsilon = 1.41$, assumes the values $J_D = 0.905$ and $J_D = 0.913$, respectively. When calculating the correlation between these VPSC and DDB results, a $J_D = 0.937$ value was obtained. This indicates that both model simulations exhibit a nearly perfect match. However, as displayed in Fig. 14, there are qualitative differences between these two textures. These differences can be observed for example in the $\{111\}\langle 211\rangle$ component, which is evidently stronger in the VPSC model than in the DDB results. Similarly, a component close to $\{111\}\langle 110\rangle$ is more developed in the DDB than in the VPSC results. These findings suggest that the quantification of ODFs difference using the texture direct correlation J_D might not capture some qualitative differences when the ODFs are analysed in terms of the intensities of specific crystallographic components. Consequently, the J_D value should be interpreted with caution, and further studies addressing the comparison of ODFs will need to be undertaken.

At this point, it is essential to clarify that a $J_D \approx 1.0$ does not necessarily imply identical ODFs, particularly when assessing specific components' intensity. Therefore, establishing a threshold value for J_D is valuable to acknowledge satisfactory alignment between the compared ODFs. Suppose a value of $J_D > 0.8$ indicates a high level of agreement. In that case, it can be concluded that most simulated DTs in this work, except FCT at $\epsilon = 1.41$, exhibit a substantial agreement with experimentally observed DTs.

6. Conclusions

This study presents a comparison of the deformation textures obtained from three mean-field crystal plasticity models (MFCP), namely

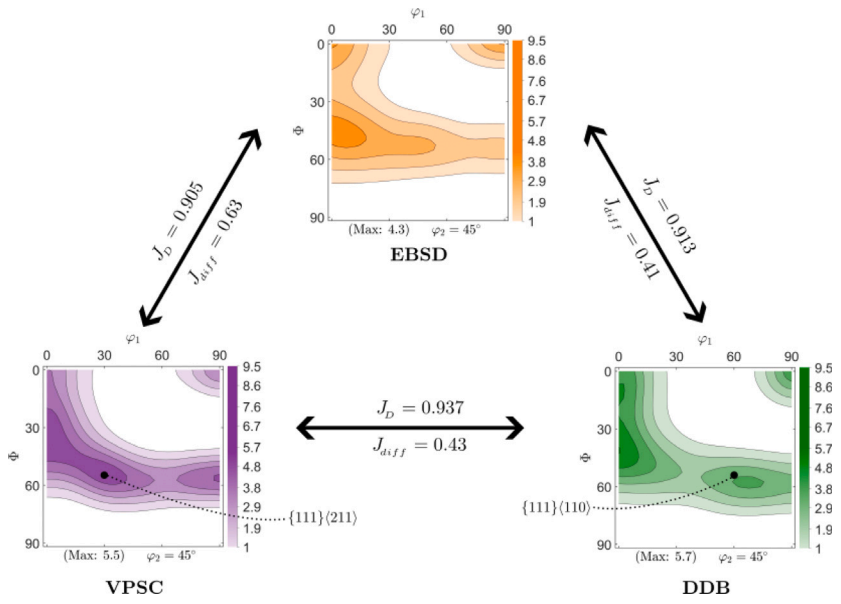

Fig. 14. VPSC, DDB and EBSD results for $\varepsilon = 1.41$, scenario-II. Texture direct correlation comparison.

the Full-constraint Taylor model(FCT), the ALAMEL model, and the Visco-Plastic Self-Consistent (VPSC) model, alongside with a full-field crystal plasticity (FFCP) dislocation-density-based (DDB) model. The comparative analysis was carried out in two scenarios: the first aimed to evaluate differences between the MFCP and DDB models, while the second assessed the disparities between the four CP models compared to the experimentally observed textures. We employed the texture direct correlation (J_D) parameter to quantitatively gauge the similarity between the ODFs. Furthermore, we conducted a qualitative analysis focusing on relevant crystallographic components and fibres. Our findings revealed that despite using the MFCP models in their simplified configurations (without grain fragmentation or strain hardening), the grain-interaction models predicted deformation texture (DT) results that reasonably matched those obtained with DDB, particularly the VPSC model. However, none of the CP models examined in this study can replicate experimentally measured DTs with absolute precision. For instance, within the $\alpha - fibre$, all CP models struggled to predict a distinctly defined rotated-cube component. In the $\gamma - fibre$ case, the MFCP models exhibited similar behaviour, showcasing high intensities for specific components in both simulation scenarios, while the DDB model appeared to favour a different component. Although all CP models generated a $\gamma - fibre$ in good alignment with experimental results, they each exhibited maximum intensities in different components compared to what was observed experimentally.

The ALAMEL and VPSC models achieved a high accuracy in predicting DT when performing simulations in their more basic configuration. These models offer a highly promising alternative for industrial applications due to their simplicity of implementation and notably reduced computational costs, which are several orders of magnitude lower compared to the Full-Field Crystal Plasticity (FFCP) models. This suggests the importance of evaluating the performance of MFCP models, including their potential grain fragmentation and strain hardening schemes. Additionally, a thorough assessment of the potential of a low-resolution DDB model in terms of accuracy compared to experimentally observed textures and computational efficiency is recommended.

One of the main differences between the MFCP and the FFCP models is that the former is better at finding a statistical solution, and the latter is better at describing grain fragmentation. Consequently, the MFCP models are expected to perform superiorly at low to intermediate strain levels, where statistical aspects of the initial texture significantly influence the predicted deformation texture. As strain increases, the impact of fragmentation becomes progressively more dominant. At high strains, irrespective of the initial texture, whether a single crystal or a random texture, the DDB model would predict the best outcomes. This phenomenon illustrates grain fragmentation's key role under high-strain conditions. Additionally, based on the research findings, comparisons at lower and medium strain levels are recommended to provide insights into the importance of grain fragmentation at lower rolling reductions.

The quantitative comparison of textures using the direct correlation coefficient, J_D, offers a reliable method for measuring the degree of difference between two textures. Nevertheless, this approach may only partially account for particular qualitative distinctions observed when the ODFs are examined concerning the intensities of particular crystallographic components. Additionally, the models used in this study can output detailed slip activity for every single deformation step of the simulations. Analysing this data could provide valuable insights into understanding crystallographic texture evolution modelling limitations and improve their prediction with crystal plasticity models.

Declaration of competing interest

The authors declare that they have no known competing financial interests or personal relationships that could have appeared to influence the work reported in this paper.

Declaration of Generative AI and AI-assisted technologies in the writing process

During the preparation of this work the author(s) used OpenAI in order to improve the readability and language of the document. After using this tool/service, the author(s) reviewed and edited the content as needed and take(s) full responsibility for the content of the publication.

Acknowledgements

This research was carried out under project number P91380 in the framework of the Partnership Program of the Materials Innovation Institute M2i (www.m2i.nl). We would like to thank Tata Steel IJmuiden for providing the specimens, and to Monika Krugla for performing the EBSD experiments for this research. J. Ochoa-Avendaño gratefully acknowledges Roberto Rocca Education Program for its support.

Appendix A. Scenario-I deformation texture results

ODF of initial texture ($\varepsilon = 0.0$) and resulting textures of rolling scenario-I for $\varepsilon = 0.22$, $\varepsilon = 0.51$, $\varepsilon = 0.91$, $\varepsilon = 1.41$ with all CP models.

	FCT	ALAMEL	VPSC	DDB
Initial texture $\varepsilon = 0.0$		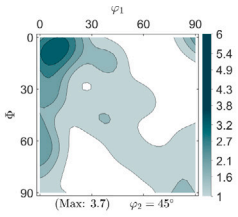		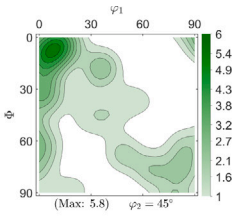
20% rolling reduction $\varepsilon = 0.22$	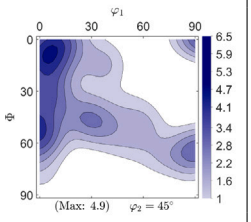	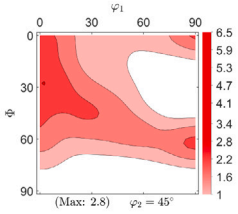	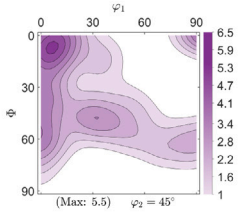	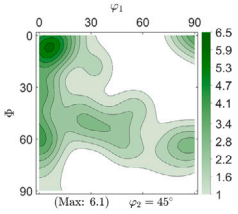
40% rolling reduction $\varepsilon = 0.51$	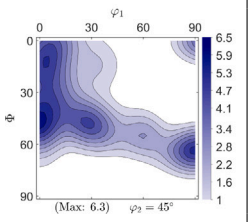	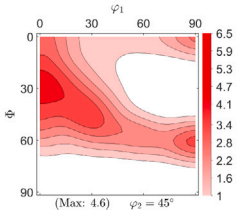	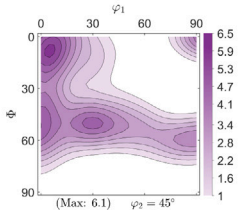	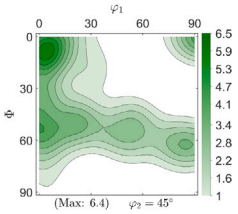
60% rolling reduction $\varepsilon = 0.91$	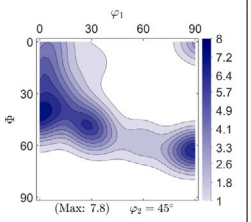	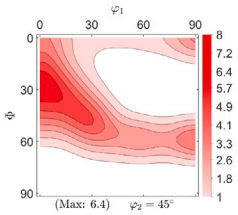	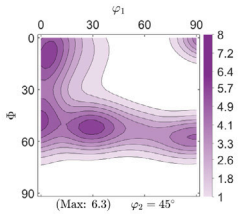	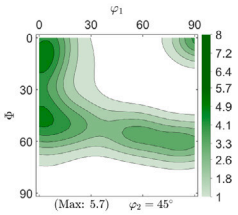
77% rolling reduction $\varepsilon = 1.41$	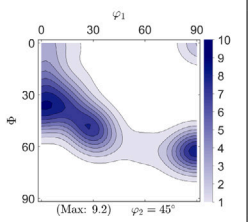	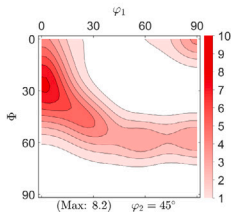	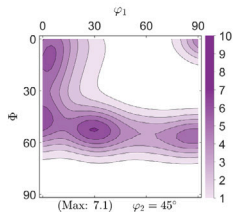	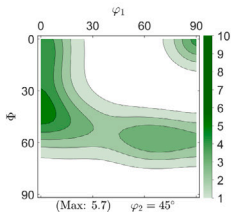

Appendix B. Scenario-II deformation texture results

ODF of initial texture ($\varepsilon = 0.0$) and resulting textures of rolling scenario-II for $\varepsilon = 0.22$, $\varepsilon = 0.51$, $\varepsilon = 0.91$, $\varepsilon = 1.41$ with all CP models, and experimentally measured textures of Hot-Rolled and Cold-Rolled 60% and 77% reduction IF-steel.

	FCT	ALAMEL	VPSC	DDB	EBSD
Initial texture $\varepsilon = 0.0$		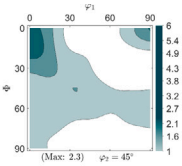		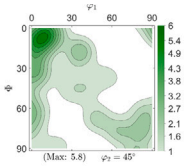	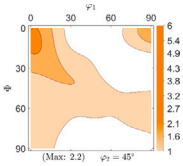
20% **rolling reduction** $\varepsilon = 0.22$	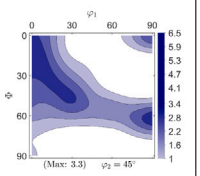	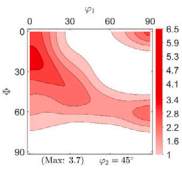	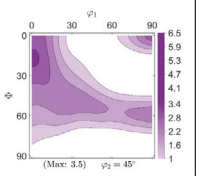	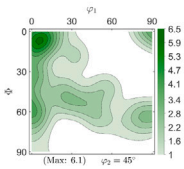	
40% **rolling reduction** $\varepsilon = 0.51$	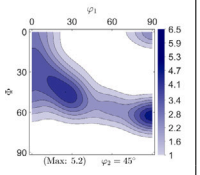	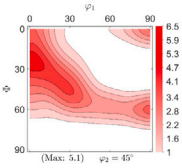	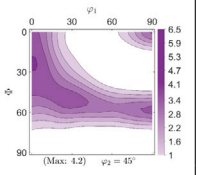	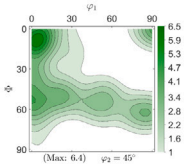	
60% **rolling reduction** $\varepsilon = 0.91$	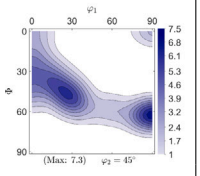	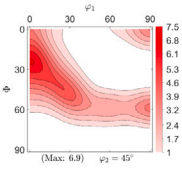	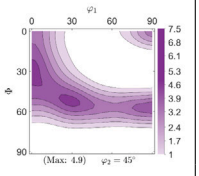	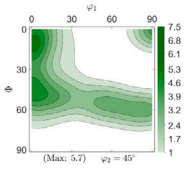	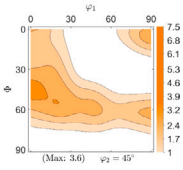
77% **rolling reduction** $\varepsilon = 1.41$	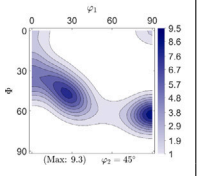	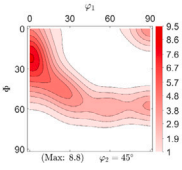	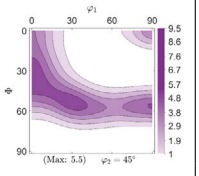	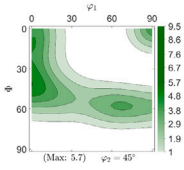	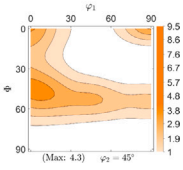

Appendix C. Scenario-I deformation texture fibres

ODFs of separated $\alpha - fibre$ and $\gamma - fibre$. Textures corresponding to $\varepsilon = 1.41$ plane strain simulations (scenario-I).

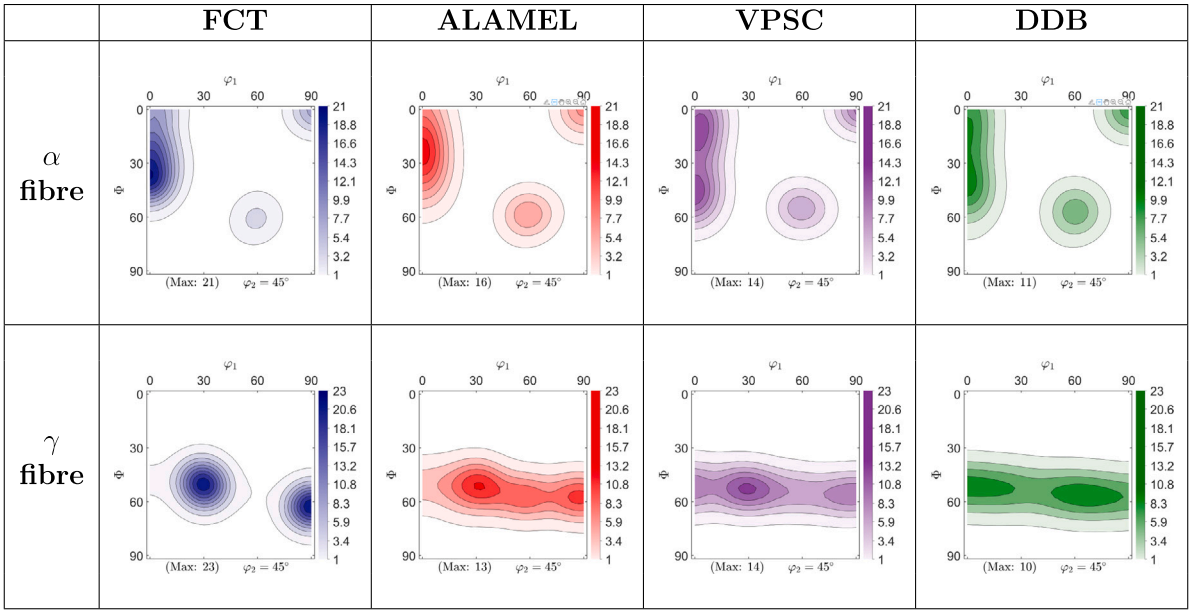

Appendix D. Scenario-II deformation texture fibres

ODFs of separated $\alpha - fibre$ and $\gamma - fibre$. Textures corresponding to $\varepsilon = 1.41$ plane strain simulations (scenario-II).

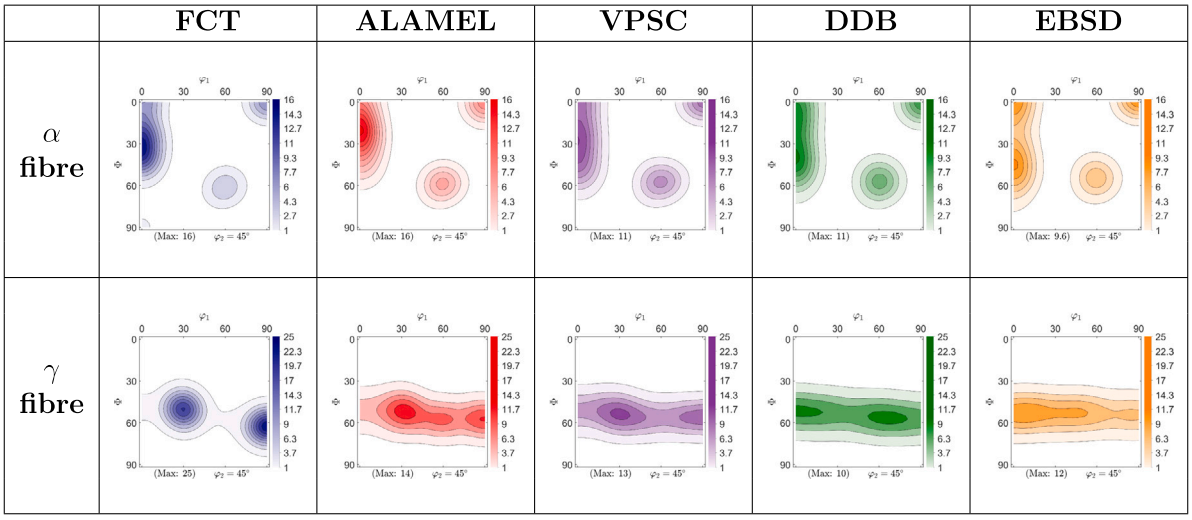

References

[1] Kestens LAI, Pirgazi H. Texture formation in metal alloys with cubic crystal structures. Mater Sci Technol 2016;32(13):1303–15. http://dx.doi.org/10.1080/02670836.2016.1231746.

[2] Nguyen-Minh T. Crystallographic texture control in a non-oriented electrical steel by plastic deformation and recrystallization (Ph.D. thesis), Delft University of Technology; 2021, http://dx.doi.org/10.4233/uuid:cff86e71-055e-47d3-bb5d-c0b73c0b3b5c.

[3] Asaro R, Needleman A. Texture development and strain hardening in rate dependent polycrystals. Acta Metall 1985;33(6):923–53. http://dx.doi.org/10.1016/0001-6160(85)90188-9.

[4] Taylor GI. Plane strain in metals. J Inst Met 1938;62:307–24.

[5] Kocks UF. A phenomenological description of crystallographic slip and pencil glide in single crystals is outlined, with emphasis on the behavior under prescribed strains. Metall Mater Trans B 1970;1:1121–43. http://dx.doi.org/10.1007/BF02900224.

[6] Van Houtte P. A comprehensive mathematical formulation of an extended Taylor–Bishop–Hill Model featuring relaxed constraints, the renouard–wintenberger theory and a strain rate sensitivity model. Textures Microstruct 1987;8:1687–5397. http://dx.doi.org/10.1155/TSM.8-9.313.

[7] Roters F, Eisenlohr P, Hantcherli L, Tjahjanto D, Bieler T, Raabe D. Overview of constitutive laws, kinematics, homogenization and multiscale methods in crystal plasticity finite-element modeling: Theory, experiments, applications. Acta Mater 2010;58(4):1152–211. http://dx.doi.org/10.1016/j.actamat.2009.10.058.

[8] Ibragimova O, Brahme A, Muhammad W, Connolly D, Lévesque J, Inal K. A convolutional neural network based crystal plasticity finite element framework to predict localised deformation in metals. Int J Plast 2022;157:103374. http://dx.doi.org/10.1016/j.ijplas.2022.103374.

[9] Roters F, Eisenlohr P, Bieler TR, Raabe D. Homogenization. In: Crystal plasticity finite element methods. Wiley; 2010, p. 93–108. http://dx.doi.org/10.1002/9783527631483.ch7.

[10] Van Houtte P. Crystal plasticity based modelling of deformation textures. In: Arunansu H, Satyam S, Debashish B, editors. Microstructure and texture in steels. London: Springer; 2009, p. 209–24.

[11] Bunge HJ. 3 - orientation distributions. In: Bunge HJ, editor. Texture analysis in materials science. Butterworth-Heinemann; 1982, p. 42–6. http://dx.doi.org/10.1016/B978-0-408-10642-9.50008-8.

[12] Kestens L, Nguyen-Minh T, Ochoa-Avendaño J, Ghiabakloo H, Van Bael A. Topological aspects of mean-field crystallographically resolved models. IOP Conf Ser: Mater Sci Eng 2022;1249(1). http://dx.doi.org/10.1088/1757-899X/1249/1/012009.

[13] Molinari A, Canova G, Ahzi S. A self-consistent approach of the large deformation polycrystal viscoplasticity. Acta Metall 1987;35(12):2983–94. http://dx.doi.org/10.1016/0001-6160(87)90297-5.

[14] Lebensohn RA, Tomé CN, Castañeda PP. Self-consistent modelling of the mechanical behaviour of viscoplastic polycrystals incorporating intragranular field fluctuations. Phil Mag 2007;87(28):4287–322. http://dx.doi.org/10.1080/14786430701432619.

[15] Solas D, Tomé C. Texture and strain localization prediction using a N-site polycrystal model. Int J Plast 2001;17(5):737–53. http://dx.doi.org/10.1016/S0749-6419(00)00030-9.

[16] Yang S, Dirrenberger J, Monteiro E, Ranc N. Representative volume element size determination for viscoplastic properties in polycrystalline materials. Int J Solids Struct 2019;158:210–9. http://dx.doi.org/10.1016/j.ijsolstr.2018.09.011.

[17] Liu B, Raabe D, Roters F, Eisenlohr P, Lebensohn RA. Comparison of finite element and fast Fourier transform crystal plasticity solvers for texture prediction. Modelling Simul Mater Sci Eng 2010;18(8). http://dx.doi.org/10.1088/0965-0393/18/8/085005.

[18] Sedighiani K, Traka K, Roters F, Raabe D, Sietsma J, Diehl M. Determination and analysis of the constitutive parameters of temperature-dependent dislocation-density-based crystal plasticity models. Mech Mater 2022;164:104117. http://dx.doi.org/10.1016/j.mechmat.2021.104117.

[19] Sedighiani K, Traka K, Roters F, Sietsma J, Raabe D, Diehl M. Crystal plasticity simulation of in-grain microstructural evolution during large deformation of IF-steel. Acta Mater 2022;237:118167. http://dx.doi.org/10.1016/j.actamat.2022.118167.

[20] Wang W, Wen W. Modeling in crystal plasticity: From theory to application. In: Caballero FG, editor. Encyclopedia of materials: metals and alloys. Oxford: Elsevier; 2022, p. 552–60. http://dx.doi.org/10.1016/B978-0-12-819726-4.00058-2.

[21] Harris WM, Chiu W. Determining the representative volume element size for three-dimensional microstructural material characterization. Part 2: Application to experimental data. J Power Sources 2015;282:622–9. http://dx.doi.org/10.1016/j.jpowsour.2015.02.052.

[22] Hutchinson W. Deformation microstructures and textures in steels. Phil Trans R Soc A 1999;357:1471–85. http://dx.doi.org/10.1098/rsta.1999.0385.

[23] Bate P, Quinta da Fonseca J. Texture development in the cold rolling of IF steel. Mater Sci Eng A 2004;380(1):365–77. http://dx.doi.org/10.1016/j.msea.2004.04.007.

[24] Van Houtte P. The MTM-FHM software system version 2, users manual. Leuven: KU Leuven; 1995.

[25] Van Houtte P, Li S, Seefeldt M, Delannay L. Deformation texture prediction: From the Taylor model to the advanced Lamel model. Int J Plast 2005;21:589–624. http://dx.doi.org/10.1016/j.ijplas.2004.04.011.

[26] Lebensohn R, Tomé C. A self-consistent viscoplastic model: prediction of rolling textures of anisotropic polycrystals. Mater Sci Eng A 1994;175(1):71–82. http://dx.doi.org/10.1016/0921-5093(94)91047-2.

[27] Roters F, Diehl M, Shanthraj P, Eisenlohr P, Reuber C, Wong S, et al. DAMASK – the Düsseldorf Advanced Material Simulation Kit for modeling multi-physics crystal plasticity, thermal, and damage phenomena from the single crystal up to the component scale. Comput Mater Sci 2019;158:420–78. http://dx.doi.org/10.1016/j.commatsci.2018.04.030.

[28] Sedighiani K, Traka K, Roters F, Sietsma J, Raabe D, Diehl M. Crystal plasticity simulation of in-grain microstructural evolution during large deformation of IF-steel. Acta Mater 2022;237:118167. http://dx.doi.org/10.1016/j.actamat.2022.118167.

[29] Bachmann F, Hielscher R, Schaeben H. Texture analysis with MTEX, free and open source software toolbox. In: Texture and anisotropy of polycrystals III. Solid state phenomena, 160, Trans Tech Publications Ltd; 2010, p. 63–8. http://dx.doi.org/10.4028/www.scientific.net/SSP.160.63.

[30] Beausir B, Fundenberger J-J. ATEX-Software Analysis tools for electron and x-ray diffraction. Metz: Université de Lorraine; 2017.

[31] C.R. Weinberger BB, Battaile C. Slip planes in bcc transition metals. Int Mater Rev 2013;58(5):296–314. http://dx.doi.org/10.1179/1743280412Y.0000000015.

[32] Takajo S, Tomé C, Vogel S, Beyerlein I. Texture simulation of a severely cold rolled low carbon steel using polycrystal modeling. Int J Plast 2018;109:137–52. http://dx.doi.org/10.1016/j.ijplas.2018.06.001.

[33] Van Houtte P. On the equivalence of the relaxed Taylor theory and the Bishop-Hill theory for partially constrained plastic deformation of crystals. Mater Sci Eng 1982;55(1):69–77. http://dx.doi.org/10.1016/0025-5416(82)90085-4.

[34] Kocks U, Chandra H. Slip geometry in partially constrained deformation. Acta Metall 1982;30(3):695–709. http://dx.doi.org/10.1016/0001-6160(82)90119-5.

[35] Xie Q, Eyckens P, Vegter H, Moerman J, Van Bael A, Van Houtte P. Polycrystal plasticity models based on crystallographic and morphologic texture: Evaluation of predictions of plastic anisotropy and deformation texture. Mater Sci Eng A 2013;581:66–72. http://dx.doi.org/10.1016/j.msea.2013.06.008.

[36] Eshelby JD. The determination of the elastic field of an ellipsoidal inclusion, and related problems. Proc R Soc A 1957;241(1226):376–96. http://dx.doi.org/10.1098/rspa.1957.0133.

[37] Saleh AA, Pereloma EV, Gazder AA. Microstructure and texture evolution in a twinning-induced-plasticity steel during uniaxial tension. Acta Mater 2013;61(7):2671–91. http://dx.doi.org/10.1016/j.actamat.2013.01.051.

[38] Galán J, Verleysen P, Lebensohn R. An improved algorithm for the polycrystal viscoplastic self-consistent model and its integration with implicit finite element schemes. Modelling Simul Mater Sci Eng 2014;22(5):055023. http://dx.doi.org/10.1088/0965-0393/22/5/055023.

[39] L. Y, Hu L, Zhou T, Yang M, Zhang J. Numerical investigation of secondary deformation mechanisms on plastic deformation of AZ31 magnesium alloy using viscoplastic self-consistent model. Metals 2019;9(1). http://dx.doi.org/10.3390/met9010041.

[40] Van Houtte P, Xie Q, Van Bael A, Sidor J, Moerman J. A new cluster-type statistical model for the prediction of deformation textures. In: Skrotzki W, Oertel C, editors. IOP conference series-materials science and engineering. Vol. 82, IOP; 2015, p. 4.

[41] Lebensohn RA, Zecevic M, Knezevic M, McCabe RJ. Average intragranular misorientation trends in polycrystalline materials predicted by a viscoplastic self-consistent approach. Acta Mater 2016;104:228–36. http://dx.doi.org/10.1016/j.actamat.2015.10.035.

[42] Zecevic M, Lebensohn RA, McCabe RJ, Knezevic M. Modeling of intragranular misorientation and grain fragmentation in polycrystalline materials using the viscoplastic self-consistent formulation. Int J Plast 2018;109:193–211. http://dx.doi.org/10.1016/j.ijplas.2018.06.004.

[43] Galán-López J, Shakerifard B, Ochoa-Avendaño J, Kestens L. Advanced crystal plasticity modeling of multi-phase steels: Work-hardening, strain rate sensitivity and formability. Appl Sci 2021;11(13). http://dx.doi.org/10.3390/app11136122.

[44] Knezevic M, McCabe RJ, Lebensohn RA, Tomé CN, Liu C, Lovato ML, et al. Integration of self-consistent polycrystal plasticity with dislocation density based hardening laws within an implicit finite element framework: Application to low-symmetry metals. J Mech Phys Solids 2013;61(10):2034–46. http://dx.doi.org/10.1016/j.jmps.2013.05.005.

[45] Kitayama K, Tomé C, Rauch E, Gracio J, Barlat F. A crystallographic dislocation model for describing hardening of polycrystals during strain path changes. Application to low carbon steels. Int J Plast 2013;46:54–69. http://dx.doi.org/10.1016/j.ijplas.2012.09.004, Microstructure-based Models of Plastic Deformation.

[46] Tomé CN, Lebensohn RA. 3 - Polycrystal viscoplasticity: theory and models. In: Tomé CN, Lebensohn RA, editors. Material modeling with the viscoplastic self-consistent (VPSC) approach. Elsevier series on plasticity of materials, Elsevier; 2023, p. 67–107. http://dx.doi.org/10.1016/B978-0-12-820713-0.00006-0.

[47] Tomé CN, Lebensohn RA. 5 - Description of viscoplastic self-consistent code and numerical algorithms. In: Tomé CN, Lebensohn RA, editors. Material modeling with the viscoplastic self-consistent (VPSC) approach. Elsevier series on plasticity of materials, Elsevier; 2023, p. 211–98. http://dx.doi.org/10.1016/B978-0-12-820713-0.00005-9.

[48] Diehl M, Wang D, Liu C, Rezaei Mianroodi J, Han F, Ma D, et al. Solving material mechanics and multiphysics problems of metals with complex microstructures using DAMASK—The Düsseldorf advanced material simulation kit. Adv Energy Mater 2020;22(3):1901044. http://dx.doi.org/10.1002/adem.201901044.

[49] Eisenlohr P, Diehl M, Lebensohn R, Roters F. A spectral method solution to crystal elasto-viscoplasticity at finite strains. Int J Plast 2013;46:37–53. http://dx.doi.org/10.1016/j.ijplas.2012.09.012, Microstructure-based Models of Plastic Deformation.

[50] Shanthraj P, Eisenlohr P, Diehl M, Roters F. Numerically robust spectral methods for crystal plasticity simulations of heterogeneous materials. Int J Plast 2015;66:31–45. http://dx.doi.org/10.1016/j.ijplas.2014.02.006.

[51] Sedighiani K, Shah V, Traka K, Diehl M, Roters F, Sietsma J, et al. Large-deformation crystal plasticity simulation of microstructure and microtexture evolution through adaptive remeshing. Int J Plast 2021;146:103078. http://dx.doi.org/10.1016/j.ijplas.2021.103078.

[52] Eisenlohr P, Roters F. Selecting a set of discrete orientations for accurate texture reconstruction. Comput Mater Sci 2008;42(4):670–8. http://dx.doi.org/10.1016/j.commatsci.2007.09.015.

[53] Lim H, Battaile CC, Bishop JE, Foulk JW. Investigating mesh sensitivity and polycrystalline RVEs in crystal plasticity finite element simulations. Int J Plast 2019;121:101–15. http://dx.doi.org/10.1016/j.ijplas.2019.06.001.

[54] Kim D-K, Kim J-M, Park W-W, Lee HW, Im Y-T, Lee Y-S. Three-dimensional crystal plasticity finite element analysis of microstructure and texture evolution during channel die compression of IF steel. Comput Mater Sci 2015;100:52–60. http://dx.doi.org/10.1016/j.commatsci.2014.09.032, 13th International Symposium on Novel and Nano Materials: ISNNM-2014.

[55] Kocks UF, Kallend JS, Biondo AC. Accurate representations of geneil textures by a set of wetghted grains. In: Textures and microstructures. Vol. 14, Gordon and Breach Science Publishers SA; 1991, p. 199–204. http://dx.doi.org/10.1155/TSM.14-18.199.

[56] Tóth LS, Van Houtte P. Discretization techniques for orientation distribution functions. Textures Microstruct 1992;19(10.1155/TSM.19.229):229–44.
[57] Pirani A. Investigation of crystallographic disorientation topology in simulation of rolling textures with the ALAMEL model. Delft University of Technology; 2021.
[58] Sedighiani K. Crystal plasticity simulation of in-grain microstructural evolution during large plastic deformation (Ph.D. thesis), Delft University of Technology; 2022, http://dx.doi.org/10.4233/uuid:38ca7b80-df99-4aae-b28d-70610229d3ed.
[59] Knezevic M, Kalidindi SR, Fullwood D. Computationally efficient database and spectral interpolation for fully plastic Taylor-type crystal plasticity calculations of face-centered cubic polycrystals. Int J Plast 2008;24(7):1264–76. http://dx.doi.org/10.1016/j.ijplas.2007.12.002.
[60] Jahedi M, Beyerlein IJ, Paydar MH, Knezevic M. Effect of grain shape on texture formation during severe plastic deformation of pure copper. Adv Energy Mater 2018;20(4):1600829. http://dx.doi.org/10.1002/adem.201600829.